Pursuant to the DOE Public Access Plan, this document represents the authors' peer-reviewed, accepted manuscript.
The published version of the article is available from the relevant publisher.

Nano Research

ISSN 1998-0124 CN 11-5974/O4
https://doi.org/10.1007/s12274-019-2590-6

Research Article

Origin of inhomogeneity in spark plasma sintered bismuth antimony telluride thermoelectric nanocomposites

Enzheng Shi[1,2,§], Shuang Cui[3,4,§], Nicholas Kempf[5], Qingfeng Xing[2], Thomas Chasapis[6], Huazhang Zhu[1], Zhe Li[1], Je-Hyeong Bahk[7], G. Jeffrey Snyder[6], Yanliang Zhang[5], Renkun Chen[3], and Yue Wu[1,2] (✉)

[1] *Department of Chemical and Biological Engineering, Iowa State University, Ames, IA 50011, USA*
[2] *Ames Laboratory, Department of Energy, Iowa State University, Ames, IA 50011, USA*
[3] *Department of Mechanical and Aerospace Engineering, University of California-San Diego, La Jolla, CA 92093, USA*
[4] *Buildings and Thermal Sciences Center, National Renewable Energy Laboratory, Golden, CO 80401, USA*
[5] *Department of Aerospace and Mechanical Engineering, University of Notre Dame, Notre Dame, IN 46556, USA*
[6] *Department of Materials Science and Engineering, Northwestern University, Evanston, IL 60208, USA*
[7] *Department of Mechanical and Materials Engineering, University of Cincinnati, Cincinnati, OH 45221, USA*

© Tsinghua University Press and Springer-Verlag GmbH Germany, part of Springer Nature 2019

Received: 21 August 2019 / **Revised:** 19 November 2019 / **Accepted:** 1 December 2019

ABSTRACT

Anisotropy and inhomogeneity are ubiquitous in spark plasma sintered thermoelectric devices. However, the origin of inhomogeneity in thermoelectric nanocomposites has rarely been investigated so far. Herein, we systematically study the impact of inhomogeneity in spark plasma sintered bismuth antimony telluride (BiSbTe) thermoelectric nanocomposites fabricated from solution-synthesized nanoplates. The figure of merit can reach 1.18, which, however, can be overestimated to 1.88 without considering the inhomogeneity. Our study reveals that the inhomogeneity in thermoelectric properties is attributed to the non-uniformity of porosity, textures and elemental distribution from electron backscatter diffraction and energy-dispersive spectroscopy characterizations. This finding suggests that the optimization of bulk material homogeneity should also be actively pursued in any future thermoelectric material research.

KEYWORDS

bismuth antimony telluride, solution synthesis, thermoelectrics, inhomogeneity

1 Introduction

Thermoelectric materials have drawn lots of attention in the recent years because they can convert waste heat into electricity and realize solid-state cooling efficiently for integrated circuits. The efficiency of thermoelectric materials can be quantified by a dimensionless figure of merit $zT = \sigma S^2 T/\kappa$ where σ, S, T and κ represent the electrical conductivity, Seebeck coefficient, absolute temperature and thermal conductivity, respectively. Most of the recent thermoelectric studies are focused on increasing zT in bulk materials, exploiting thermoelectric materials composed of earth-abundant elements, and flexible thermoelectrics [1–15].

Due to the crystal symmetry, lots of thermoelectric single crystals or ingots show anisotropic σ, S, and κ, such like hexagonal Bi_2Te_3 based solid solutions [16] and orthorhombic SnSe [4, 5]. In addition, polycrystal Bi_2Te_3 and SnSe samples sintered from ball-milling [17–19], solution-synthesis [20–23] and melt-spinning [1] nanomaterials are also anisotropic owing to the formation of textures during sintering. The anisotropy must be taken into consideration because there is huge discrepancy if the σ, S, and κ are obtained along different directions. Similarly, the spatial inhomogeneity in thermoelectric samples is also inevitable due to phase separation and gravity during solid-state reaction and material processing, which could further result in the over- or under- estimation of zT value. For instance, S of BiSbTe samples shows dependence of spatial locations due to the temperature gradient during spark plasma sintering (SPS) process [24]. And the macroscopic inhomogeneity has also been found in $(AgSbTe_2)_x(PbTe)_{1-x}$ due to the formation of multiphase on the scale of millimetres [25]. Recently, solution synthesis of thermoelectric materials draws increasing attention as a new approach to control doping and grain size [23, 26, 27]. However, residual surfactants in the nanomaterials can be transformed into carbon or other impurities, as well as micrometer-sized pores within the sintered thermoelectric nanocomposites [20, 22]. This may potentially result in spatial inhomogeneity and discrepancy of final zT determination. However, the inhomogeneity of bulk thermoelectric nanocomposites and its corresponding origin has been rarely investigated so far.

In this report, we systematically studied the inhomogeneity in solution-synthesized bismuth antimony telluride (BiSbTe) bulk nanostructured composite disks prepared by SPS. The compositional and structural inhomogeneity were investigated by scanning electron microscopy (SEM), energy dispersive spectroscopy (EDS) elemental mapping and electron backscatter diffraction (EBSD) mapping. By comparing the σ, S and power factor (PF) of one BiSbTe disk and a smaller bar diced from the identical disk, the effect of inhomogeneity on thermoelectric performance has been clearly demonstrated. The thermal conductivity κ of the bar was measured by the 3ω method, yielding a value of 0.67–0.78 W/(m·K) as a function of temperature.

Address correspondence to yuewu@iastate.edu

Pursuant to the DOE Public Access Plan, this document represents the authors' peer-reviewed, accepted manuscript.
The published version of the article is available from the relevant publisher.

The highest zT of our sample is 1.18 whereas could be overestimated to 1.88 without considering the inhomogeneity. Our study reveals that the inhomogeneity is attributed to the non-uniformity of grain orientation and elemental distribution within the thermoelectric nanocomposites.

2 Results and discussion

The solution synthesis process of BiSbTe nanoplates is described in the Method. The intermediate product after 100 °C reaction for 1 h was indexed as pure phase tellurium (Te) based on X-ray diffraction (XRD) pattern (Fig. S1 in the Electronic Supplementary Material (ESM)). The transmission electron microscopy (TEM) and SEM images (Figs. 1(a) and 1(b) and Fig. S1 in the ESM) show that the Te nanowires are uniform with a diameter of 6 ± 0.7 nm and a length of 1.54 ± 0.06 μm. In addition, the clear lattice fringes in the high-resolution TEM (HRTEM) image show that the Te nanowires are highly crystallized and the nanowire is parallel to (100) plane and perpendicular to (001) plane, suggesting the growth direction is along c axis due to its trigonal crystal structure [23, 28]. Besides, the low reaction temperature also favors the formation of one-dimensional nanowires [29]. The final product is identified as $Bi_{0.5}Sb_{1.5}Te_3$ (BiSbTe, Fig. S2 in the ESM). The morphology and structure of BiSbTe are characterized by SEM and TEM, showing BiSbTe nanoplates with lateral diameter ranging from 50 to 500 nm (Fig. S2 in the ESM) and the thickness between 3 to 6 nm, containing 3–6 quintuple layers, determined by the TEM images of cross-sectional BiSbTe plates (Fig. S3 in the ESM). The hexagonal shape of BiSbTe nanoplate is consistent with its hexagonal structure and space group (166) $R\bar{3}m$. From the selected-area-electron-diffraction (SAD) pattern (inset in Fig. 1(d)) of BiSbTe nanoplate, the 6 brightest diffraction dots correspond to a group of crystal planes of (110), (100), (010), $(\bar{1}\bar{1}0)$, $(\bar{1}00)$ and $(0\bar{1}0)$, which indicates the nanoplate is perpendicular to c axis and is also consistent with the (003) crystal plane identified from the TEM images of cross-sectional BiSbTe nanoplate (Fig. S3 in the ESM).

Our spark plasma sintered (SPSed) BiSbTe samples show obvious anisotropy and inhomogeneity. As is shown in Figs. 2(a) and 2(b), one BiSbTe disk (Φ 10 mm × 1.5 mm) was diced into a BiSbTe rectangular bar. The BiSbTe bar had a length of 7.9 mm, a width of 1.1 mm and the same thickness with the pristine disk. After the SPS, the position of XRD peaks remained almost identical with the as-synthesized nanoplates (Fig. 2(c)). However, the width of the peaks apparently decreases, indicating the ripening of nanoplates during sintering. In addition, the XRD spectrum in Fig. 2(c) shows enhanced peaks for (006), (0015) and (0018) crystal planes, while that from cross-plane direction shows enhanced peak for (110) crystal plane (Fig. S5(a) in the ESM). This indicates the preferential arrangement of BiSbTe grains and anisotropy of our SPSed BiSbTe nanoplate composite sample.

The in-plane σ and S for the disk and bar are compared in Figs. 2(d) and 2(e). The σ decreases monotonically as the temperature increases from 300 to 475 K, which was a typical characteristic for a heavily doped degenerate semiconductor. For the bar, the σ at 313 K was 6.3×10^4 S/m, while the σ of the disk is as large as 9.6×10^4 S/m, over 50% larger than that of the bar. From Fig. 2(e), the positive S reveals that our sample is p-type. The S of the BiSbTe disk increases from 198 μV/K at 300 K to its maxima (215 μV/K) at 395 K, and decreases back to 200 μV/K at 473 K. The analysis of the data indicated the following issues: (1) The dramatic difference in the electrical conductivity could be a sign of the inhomogeneity in the SPSed BiSbTe disk, directly leading to the σ difference spatially from

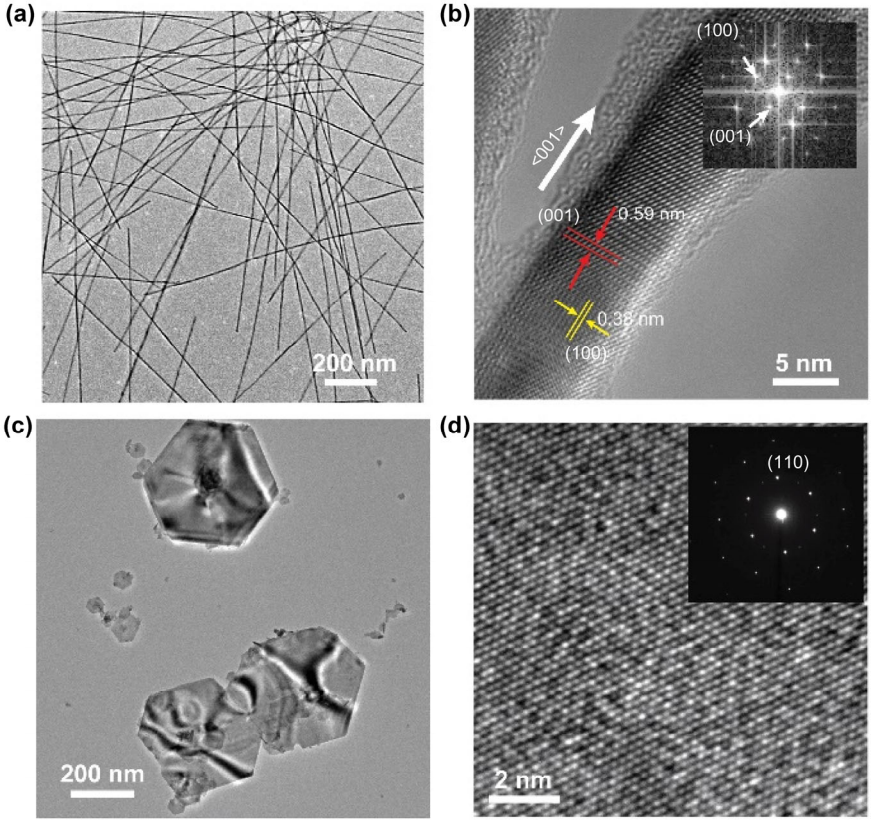

Figure 1 TEM images of solution-synthesized Te nanowires and BiSbTe nanoplates. (a) TEM image of Te nanowires. (b) HRTEM image of Te nanowire, the inset represents the FFT pattern of the Te nanowire. (c) TEM image of BiSbTe nanoplates. (d) HRTEM image of BiSbTe nanoplate, and the inset represents the corresponding SAD pattern.

Pursuant to the DOE Public Access Plan, this document represents the authors' peer-reviewed, accepted manuscript.
The published version of the article is available from the relevant publisher.

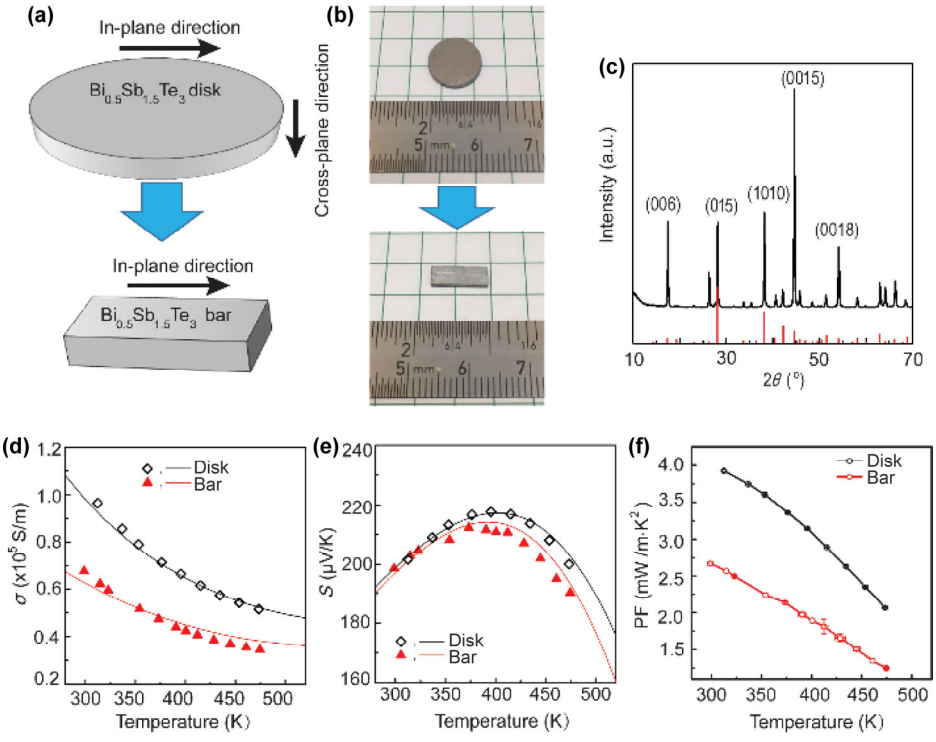

Figure 2 BiSbTe thermoelectrics. (a) and (b) Schematic and optical images of BiSbTe bar fabrication process. (c) XRD pattern of in-plate BiSbTe sample. (d) and (e) Comparison of σ and S of BiSbTe disk and bar. Isolated squares and triangles represent the experimental values and the continuous plots represent theoretical calculation results. (f) Comparison of PF of BiSbTe disk and bar.

edge to the center of the round disk; (2) the trend in Seebeck coefficient suggests a typical behavior of bipolar conduction. With the increase of temperature, both majority (holes) and minority (electrons) carriers contribute to S, leading to a parabolic dependence of S with temperature. The S of the bar go through similar dependence of measurement temperature but the difference between the BiSbTe disk and bar in S is not significant. In Figs. 2(d) and 2(e), the isolated black squares and red triangles represent the experimental σ and S while the continuous plots represent the theoretical results. As we can see, both σ and S fit very well using the electron transport model [30]. For σ modeling, stronger short-range defect scatterings have been added to account for the reduced carrier mobility and thus σ in bar, which can be due to the higher porosity, increased interfaces density, and imperfect crystal structure. At the same time, this has almost negligible effect on S because S is predominantly determined by the band structure and the Fermi level position. More information about the electron transport modeling can be found in the ESM.

The power factor, PF = σS^2, in Fig. 2(f) shows an obvious difference between BiSbTe disk and bar, where the maximum PF of the disk can reach 3.92 mW/(m·K^2) at 312 K, while the PF of the BiSbTe bar at 314 K is only 2.56 mW/(m·K^2), a reduction of about 35% mostly due to the reduced carrier mobility. As zT is linearly related to PF at a certain thermal conductivity, it is essential to measure the PF and thermal conductivity at the same sample to avoid the confusion induced by inhomogeneity. We will discuss the thermal conductivity later.

Besides, our sintered BiSbTe samples show apparent anisotropy, which means that the in-plane thermoelectric parameters, including σ, κ and S, are different from those in cross-plane direction. This anisotropy has already been discussed in many literatures. By increasing the amount of BiSbTe dry powders into the graphite die, BiSbTe cylinders with a height of 10 mm and a diameter of 10 mm can be obtained (Fig. S6(a) in the ESM). The σ, κ and S in both directions were all measured and presented in Fig. S6 in the ESM. It is clearly demonstrated that these parameters have a substantial difference in the in-plane and cross-plane directions. And the calculated zT is 0.94 and 0.58 for in-plane and cross-plane directions, respectively. The anisotropy can be directly exhibited from the XRD spectra as shown in Fig. S5(a) in the ESM. In addition, the SEM images (Figs. S5(b)–S5(e)) also reveals the different orientations of grains in both directions.

After the BiSbTe disk is polished by sandpaper, diamond slurry and argon ion milling, the surface becomes smooth enough so that the grain boundaries can be distinguished from the high-magnification SEM studies (Fig. 3(a) in the ESM). Although the SPS time at 480 °C is restricted to only 3 min, it is obvious that the pristine nanoplate disappears after SPS and the grain size increases to several micrometers (Figs. 3(a) and 3(d)). The grain orientation and size were measured by EBSD mapping, where we use the standard crystallographic information (cif) file for $Bi_{0.4}Sb_{1.6}Te_3$ to stand for our $Bi_{0.5}Sb_{1.5}Te_3$ sample, because they have the same crystal structure and very close lattice constant (the lattice constant difference is within 1% between $Bi_{0.4}Sb_{1.6}Te_3$ and $Bi_{0.5}Sb_{1.5}Te_3$). The EBSD mapping (Fig. 3(b)) for a typical in-plane surface reveals that our BiSbTe sample is highly textured with most of planes close to (001) plane, which is consistent with XRD results (Fig. S5 in the ESM). Black dots herein are probably pores or amorphous carbon which cannot be identified as standard crystal planes in $Bi_{0.4}Sb_{1.6}Te_3$. The grain size distribution (Fig. 3(c)) is also summarized from the EBSD mapping. Most of the grains have a size between 2 to 5 μm, and the calculated average grain size is 4.2 μm. Most of the surfactants have been removed by repeated rinsing. However, it must be pointed out that lots of carbon is still found in the sintered disk, especially between adjacent grains (Figs. S7 and S8 in the ESM). The source of carbon is likely to come from the residue PVP on the surface of solution-synthesized BiSbTe nanoplates. This directly results in the smaller mass density of our BiSbTe

Pursuant to the DOE Public Access Plan, this document represents the authors' peer-reviewed, accepted manuscript.
The published version of the article is available from the relevant publisher.

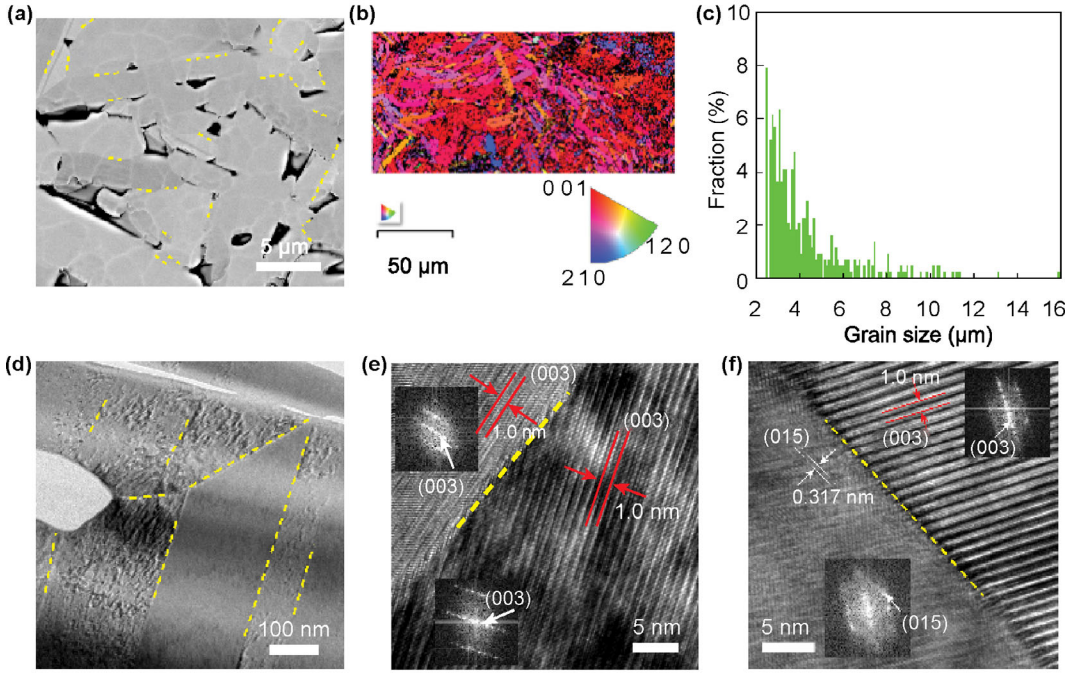

Figure 3 Structural characterization of SPSed BiSbTe sample. (a) SEM image of in-plane BiSbTe sample. (b) EBSD mapping image showing the size and orientation of BiSbTe grains. (c) The distribution of BiSbTe grain size obtained from EBSD results. (d) TEM image of FIB-cut BiSbTe sample. (e) and (f) HRTEM images of BiSbTe showing the grain boundary of BiSbTe grains with different orientations. The yellow dashed lines indicate the traces of grain boundaries.

disks, which is only 5.7–6.1 g/cm^3, about 83%–89% of the theoretical value of single crystal. The pores, partially filled with carbon (Figs. 3(a) and 3(b)), will also lower the thermal conductivity [22], which should be beneficial in the improvement of thermoelectric performance. The HRTEM images in Figs. 3(e) and 3(f) also show highly crystallized BiSbTe within the grains. As the TEM sample was fabricated by focused ion beam (FIB) method from an in-plane BiSbTe sample, the observed plane is parallel to the disk's cross-plane direction. Therefore, it is easier to find lots of grains are perpendicular to the *a*-*b* plane and it is consistent with the XRD pattern in Fig. S5(a) in the ESM.

We employed the 3ω method to measure the in-plane κ of the BiSbTe bars [31]. We have used the same setup in our previous study [32], in which the method was calibrated using a Si covered by 60 nm thick Al_2O_3 sample. The 3ω method is typically more suitable to measure the cross-plane κ of bulk samples. To measure the κ along the in-plane direction in the bars, which is also the direction where we have performed the electrical conductivity and Seebeck measurements, we cut the bars and deposited the 3ω heaters on the side wall of the bars, as shown schematically in Fig. 4(a). With this approach, the normal cross-plane 3ω measurement would yield the in-plane κ of the bars. Figure 4(b) shows a photograph of a chip carrier

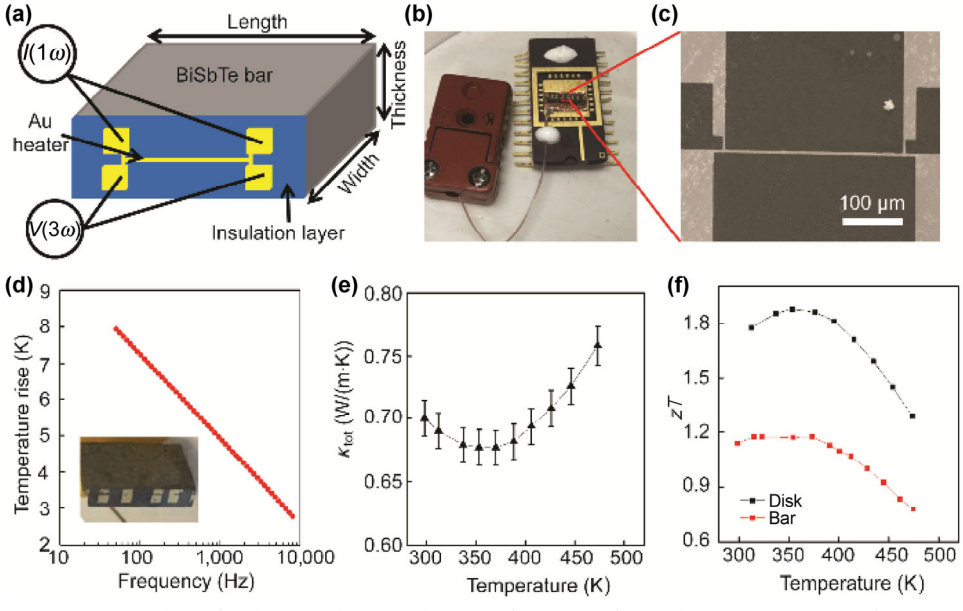

Figure 4 In-plane κ measurement and zT of BiSbTe samples. (a) Schematic of 3ω device for in-plane κ measurement of BiSbTe bar. (b) Optical image of 3ω device for κ measurement of BiSbTe bar. (c) SEM image of 3ω heater. (d) Temperature rise as a function of frequency during 3ω measurement. (e) Measured in-plane κ of BiSbTe bar. (f) Comparison of zT values based on the measured PFs for BiSbTe disk and bar and κ of BiSbTe bar.

Pursuant to the DOE Public Access Plan, this document represents the authors' peer-reviewed, accepted manuscript.
The published version of the article is available from the relevant publisher.

containing a bar with 3ω heaters deposited on the side wall, which was facing up when mounted to the chip carrier. We also attached a thermocouple to the sample to accurately measure the sample temperature. The 3ω heaters were fabricated by standard microfabrication processes, including photolithography, metal evaporation, and lift off. The metal heaters are made of Cr (30 nm)/Au (150 nm) and are 300 nm in length and 5 μm in width (Figs. 4(b) and 4(c)). We also deposited a 600 nm thick parylene layer on top of the BiSbTe bar to electrically insulate the samples from the 3ω metal heaters.

During the 3ω measurements, the heater functions both as a heater for applying a periodic heat flux and a thermometer for measuring the surface temperature. An AC current, I_ω, modulated at an angular modulation frequency ω, was applied to the heater, leading to a heat flux oscillating at 2ω

$$P = [I_0 \sin(\omega t)]^2 R = \frac{I_0^2 R}{2} - \frac{I_0^2 R}{2}\cos(2\omega t) \quad (1)$$

which includes a DC component and a 2ω component. The latter leads to a temperature rise also oscillating at 2ω ($\Delta T_{2\omega}$) with a phase shift ϕ. Since the resistance change of the heater is proportional to the temperature change, the resistance will also oscillate at 2ω, which leads to a third harmonic voltage ($V_{3\omega} = I_\omega R_{2\omega}$)

$$V_{3\omega} = \frac{I_0}{2}\frac{dR}{dT}\Delta T_{2\omega}\sin(3\omega t + \phi) \quad (2)$$

Therefore, the measured $V_{3\omega}$ can be used to extract the $\Delta T_{2\omega}$. The cross-plane κ of the sample, which is the in-plane κ of the BiSbTe bars, can be obtained by fitting the slope of $\Delta T_{2\omega}$ vs. ln(2ω) curve (Fig. 4(d)) [33].

$$K_{BST} = -\frac{P}{2\pi L}\left(\frac{d(\Delta T_{2\omega})}{d(\ln(2\omega))}\right)^{-1} \quad (3)$$

Figure 4(e) shows that the measured in-plane κ in the BiSbTe bars from 300 to 473 K. The measured κ is 0.70 ± 0.014 W/(m·K) at 299 K. It decreases to 0.68 ± 0.014 W/(m·K) at 353 K and then increases to 0.76 ± 0.015 W/(m·K) at 473 K. The error bar represents the uncertainties in the measurement, which mainly comes from the temperature measurement and the determination of the temperature coefficient of resistance (TCR) of the 3ω heaters.

Based on the PF and in-plane κ of the BiSbTe bar, the zT of the bar can be determined, which is over 1.1 from 299 to 401 K, as shown in Fig. 4(f). The maximum zT is 1.18 at 373 K. However, if we assumed our BiSbTe sample is 100% uniform and homogeneous, the zT of the disk can be determined by using the PF of the disk and the κ of the bar, and the maximum

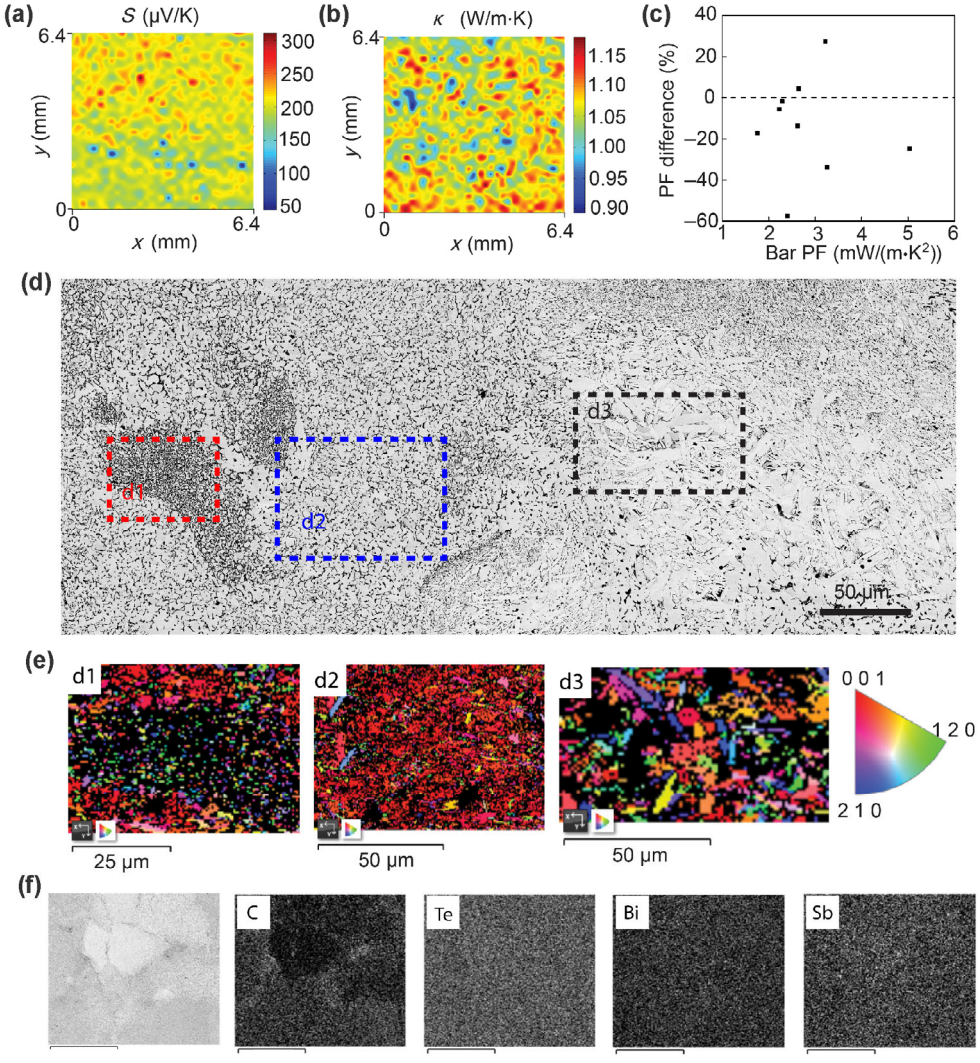

Figure 5 Inhomogeneity in SPSed BiSbTe samples. (a) and (b) Large-scale S and κ mapping of a BiSbTe disk in in-plane direction. (c) PF differences between BiSbTe disk and bar for nine samples. (d) Back-scattering SEM image of in-plane BiSbTe sample showing the inhomogeneity of porosity. Three rectangular areas marked as d1, d2 and d3 was analyzed by EBSD mapping in (e). (e) EBSD mappings of d1, d2 and d3 in (d) showing the inhomogeneity of textures. (f) Elemental mapping of in-plane BiSbTe disk over a large area, showing the compositional inhomogeneity. The scale bars are 250 μm.

Pursuant to the DOE Public Access Plan, this document represents the authors' peer-reviewed, accepted manuscript.
The published version of the article is available from the relevant publisher.

value can be as large as 1.88. This huge zT overestimation also implies the importance of inhomogeneity.

To confirm the existence of thermoelectric inhomogeneity more straightforwardly, we have also performed Seebeck coefficient and thermal conductivity mapping (Figs. 5(a) and 5(b)) for one round BiSbTe disk (Φ = 10 mm) over a large surface area. The experimental mapping details were reported previously [34]. The mapping area is 6.4 mm × 6.4 mm with 33 × 33 grids for 1,089 measurements in total. The grid spacing is 200 μm and the spatial resolution of each measurement is approximately 5 μm. The high porosity in our samples will introduce some variance that may affect the absolute value of S and κ. However, the measured values from various locations can still qualitatively demonstrate the inhomogeneity. There is a big fluctuation of S as shown in Fig. 5(a), varying from 50 to 300 μV/K, and the average S is calculated to be 201.3 μV/K, which was ~ 97% of the bulk S value (Fig. S10 in the ESM) measured at room temperature. And the κ mapping also shows apparent spatial inhomogeneity in our sample. The κ varies from 0.9 to above 1.1 W/(m·K) at different locations, and the average is 1.06 W/(m·K).

To demonstrate the universality of the spatial inhomogeneity discussed above in our SPSed BiSbTe samples, PF difference ratio is defined as follows, to quantify the spatial inhomogeneity of BiSbTe disks

$$\text{PF difference ratio} = \frac{\text{PF}_{\text{bar}} - \text{PF}_{\text{disk}}}{\text{PF}_{\text{bar}}} \quad (4)$$

where PF_{disk} and PF_{bar} are the PF for the BiSbTe disk and bar. The PF difference ratio is plotted as a function of PF_{bar} in Fig. 5(c). Total nine BiSbTe disks were diced into bars and the in-plane PF values were measured for these disks and bars, respectively. The PF for these bars ranges from 1.7 to 5.1 mW/(m·K^2), while the PF for these corresponding disks ranges from 2.0 to 6.2 mW/(m·K^2). The PF difference ratio ranges from −60% to 30%, most of which are larger than 10%, which indicates the spatial inhomogeneity universally exists in most of the SPSed samples.

The inhomogeneity in thermoelectric properties originates from the structural (porosity and textures) and compositional inhomogeneity. From the low-magnification SEM image of the BiSbTe bar (Fig. 5(d)), where dark areas represent pores, the distribution of pores is non-uniform, resulting in a structural inhomogeneity. The porosity in areas d1, d2 and d3 is different, and area d1 has the highest porosity while area d3 is most densified. In addition, we have performed EBSD mapping for these 3 areas, as shown in Fig. 5(e). It is shown that the textures in area d2 are consistent with that of Fig. 3(b), where the preferential orientation of grains is (001). However, most of detected grains are along (120) in the dark areas of d1 and the grains are randomly orientated in area d3. This implies the non-uniformity of textures in different domains is also a structural origin of the thermoelectric inhomogeneity. In addition to the non-uniformity of pores and textures, Fig. 5(f) and Figs. S7–S9 in the ESM also indicate that carbon tends to accumulate between adjacent grains and areas with higher porosity, thus leading to the compositional non-uniformity.

3 Conclusions

To conclude, we have demonstrated the solution synthesis of BiSbTe nanoplate-based nanocomposite with high thermoelectric performance. Careful investigation in SPSed BiSbTe nanocomposite samples suggested that the inhomogeneity can cause a big fluctuation in local electrical conductivity, Seebeck coefficient, and thermal conductivity, as resulted from structural (including porosity and textures) and compositional non-uniformity. Our study provides fundamental insights for better understanding the significance of inhomogeneity in thermoelectric nanocomposites, and technologically suggests that more reliable performance of thermoelectric nanocomposites can be achieved if the inhomogeneity is fully suppressed.

4 Methods

4.1 Synthesis of $Bi_{0.5}Sb_{1.5}Te_3$ nanoplates

The solution synthesis of $Bi_{0.5}Sb_{1.5}Te_3$ nanoplates consisted of the following steps. Firstly, 7.182 g of tellurium dioxide (TeO_2, 99%+, Sigma-Aldrich), 450 mL of ethylene glycol (EG, 99%+, VWR International Ltd.), 33.66 g of potassium hydroxide flakes (KOH, 90%, Sigma-Aldrich), and 9.0 g of polyvinylpyrrolidone (PVP, average molecule weight 40,000 g/mol, Sigma-Aldrich) were added in a three-neck 1-liter flask. Afterwards, the flask was placed on a digitally controlled heating mantle with a magnetic bar stirring the solution uninterruptedly. When the temperature of the solution reached 100 °C, 10 mL of anhydrous hydrazine (N_2H_4, Sigma-Aldrich) was injected into the flask. Meanwhile, nitrogen was purged and the reaction was kept at 100 °C for 1 h, during which 3.638 g of $Bi(NO_3)_2{\cdot}5H_2O$ (99.99%+, Sigma-Aldrich) and 6.725 g of $Sb(CH_3COO)_2$ were dissolved in 100 mL of EG as bismuth and antimony precursors on a 140 °C hot plate. Thereafter, the flask was heated to 110 °C and another 10 mL of anhydrous hydrazine was injected rapidly into the reaction. The flask was continuously heated to 140 °C and the 100 mL of bismuth and antimony precursors was injected dropwise into the flask. The reaction was kept at 140 °C for 12 h under a nitrogen atmosphere and cooled down naturally to room temperature finally. The volume of as-synthesized BiSbTe nanoplates solution was about 600 mL (Fig. S1(a) in the ESM).

4.2 Purification of BiSbTe nanoplates

During the synthesis of BiSbTe nanoplates, PVP was used as surfactants to avoid the aggregation of the nanoplates. To remove the PVP surfactants, we washed and centrifuged the as-synthesized BiSbTe nanoplates three times and the nanoplate precipitates were then vigorously stirred in ethanol/hydrazine solution for 24 h. After the hydrazine solution rinsing, the nanoplates were collected by centrifugation and kept in a vacuum chamber to evaporate all residual ethanol. The final dry BiSbTe powder for each reaction was about 9.7 g in mass (Fig. S4 in the ESM) with an impressive high yield of 97%.

4.3 SPS of BiSbTe nanocomposites

The dry BiSbTe powders were pulverized in agate mortar and then loaded into graphite die with two graphite punches (Φ = 10 mm) sealing two sides in nitrogen glovebox. Afterwards, the graphite die was transferred into the chamber of a Fuji-211lx SPS system. Then the chamber was pumped into vacuum (as low as 6 Pa) and an upright uniaxial pressure of 50 MPa was applied between two graphite punches. The SPS system was heated to 480 °C in 11 min and kept for 3 min. The SPSed BiSbTe disk has a diameter of 10 mm and a thickness of 1.5–3 mm. From the EDS results (Table S1 in the ESM), the Bi:Sb:Te atomic ratio is determined to be 0.58:1.51:3, which is very close to the stoichiometric ratio of precursors (0.5:1.5:3).

4.4 Characterization and measurement

The morphology, micro-structure and EDS elemental mapping

Pursuant to the DOE Public Access Plan, this document represents the authors' peer-reviewed, accepted manuscript.

of BiSbTe samples were characterized by SEM (FEI Quanta 250 FE-SEM) and TEM (FEI Tecnai G2-F20). Electrical conductivity and Seebeck coefficient measurement were performed on Linseis LSR-3 system. EBSD mapping was performed on FEI Teneo field emission SEM. The in-plane thermal conductivity of the BiSbTe bar was measured by 3ω method.

Acknowledgements

R. K. C. acknowledges grant # NSF(DMR-1508420). Y. W. thanks the support from the Herbert L. Stiles Professorship and ACRI Center Initiative from Iowa State University.

Electronic Supplementary Material: Supplementary material (electron transport modeling for BiSbTe samples; additional morphology and structural characterizations of BiSbTe nanoplates, Te nanowires, SPSed BiSbTe samples; the anisotropy of SPSed BiSbTe etc) is available in the online version of this article at https://doi.org/10.1007/s12274-019-2590-6.

Dedication

Yue Wu joined Prof. Charles M. Lieber's group in July 2001 for Ph.D. study after receiving bachelor's degree from University of Science and Technology of China. In the Lieber group, his research was focusing on the following areas: (1) self-assembly of silicon nanowires; (2) metal-semiconductor nanowire heterostructures between silicon and metal silicides for short-channel nanowire transistors/sensors; (3) atomic layer deposition of high-*k* dielectric oxides and ferroelectric oxides to create silicon-multifunctional oxide heterostructures for high-performance nanowire transistors and memory/logic circuits. Wu graduated from the Lieber group in June 2006 and headed to University of California of Berkeley for postdoc. In 2009 Wu started as assistant professor in School of Chemical Engineering at Purdue University. In 2014 Wu received an early promotion to tenure associate professor, then moved to Iowa State University as Herbert L. Stiles associate professor of chemical and biological engineering.

References

[1] Kim, S. I.; Lee, K. H.; Mun, H. A.; Kim, H. S.; Hwang, S. W.; Roh, J. W.; Yang, D. J.; Shin, W. H.; Li, X. S.; Lee, Y. H. et al. Dense dislocation arrays embedded in grain boundaries for high-performance bulk thermoelectrics. *Science* **2015**, *348*, 109–114.

[2] Biswas, K.; He, J. Q.; Blum, I. D.; Wu, C. I.; Hogan, T. P.; Seidman, D. N.; Dravid, V. P.; Kanatzidis, M. G. High-performance bulk thermoelectrics with all-scale hierarchical architectures. *Nature* **2012**, *489*, 414–418.

[3] Korkosz, R. J.; Chasapis, T. C.; Lo, S. H.; Doak, J. W.; Kim, Y. J.; Wu, C. I.; Hatzikraniotis, E.; Hogan, T. P.; Seidman, D. N.; Wolverton, C. et al. High ZT in p-type $(PbTe)_{1-2x}(PbSe)_x(PbS)_x$ thermoelectric materials. *J. Am. Chem. Soc.* **2014**, *136*, 3225–3237.

[4] Zhao, L. D.; Tan, G. J.; Hao, S. Q.; He, J. Q.; Pei, Y. L.; Chi, H.; Wang, H.; Gong, S. K.; Xu, H. B.; Dravid, V. P. et al. Ultrahigh power factor and thermoelectric performance in hole-doped single-crystal SnSe. *Science* **2016**, *351*, 141–144.

[5] Zhao, L. D.; Lo, S. H.; Zhang, Y. S.; Sun, H.; Tan, G. J.; Uher, C.; Wolverton, C.; Dravid, V. P.; Kanatzidis, M. G. Ultralow thermal conductivity and high thermoelectric figure of merit in SnSe crystals. *Nature* **2014**, *508*, 373–377.

[6] Biswas, K.; Zhao, L. D.; Kanatzidis, M. G. Tellurium-free thermoelectric: The anisotropic n-type semiconductor Bi_2S_3. *Adv. Energy Mater.* **2012**, *2*, 634–638.

[7] Zhao, L. D.; Berardan, D.; Pei, Y. L.; Byl, C.; Pinsard-Gaudart, L.; Dragoe, N. $Bi_{1-x}Sr_xCuSeO$ oxyselenides as promising thermoelectric materials. *Appl. Phys. Lett.* **2010**, *97*, 092118.

[8] Liu, Y.; Zhao, L. D.; Liu, Y. C.; Lan, J. L.; Xu, W.; Li, F.; Zhang, B. P.; Berardan, D.; Dragoe, N.; Lin, Y. H. et al. Remarkable enhancement in thermoelectric performance of BiCuSeO by Cu deficiencies. *J. Am. Chem. Soc.* **2011**, *133*, 20112–20115.

[9] Ren, G. K.; Wang, S. Y.; Zhu, Y. C.; Ventura, K. J.; Tan, X.; Xu, W.; Lin, Y. H.; Yang, J. H.; Nan, C. W. Enhancing thermoelectric performance in hierarchically structured BiCuSeO by increasing bond covalency and weakening carrier–phonon coupling. *Energy Environ. Sci.* **2017**, *10*, 1590–1599.

[10] Ge, Z. H.; Zhang, B. P.; Chen, Y. X.; Yu, Z. X.; Liu, Y.; Li, J. F. Synthesis and transport property of $Cu_{1.8}S$ as a promising thermoelectric compound. *Chem. Commun.* **2011**, *47*, 12697–12699.

[11] He, Y.; Day, T.; Zhang, T. S.; Liu, H. L.; Shi, X.; Chen, L. D.; Snyder, G. J. High thermoelectric performance in non-toxic earth-abundant copper sulfide. *Adv. Mater.* **2014**, *26*, 3974–3978.

[12] Liang, L. R.; Chen, G. M.; Guo, C. Y. Polypyrrole nanostructures and their thermoelectric performance. *Mater. Chem. Front.* **2017**, *1*, 380–386.

[13] Liu, L. Y.; Sun, Y. H.; Li, W. B.; Zhang, J. J.; Huang, X.; Chen, Z. J.; Sun, Y. M.; Di, C. G.; Xu, W.; Zhu, D. B. Flexible unipolar thermoelectric devices based on patterned poly[K_x(Ni-ethylenetetrathiolate)] thin films. *Mater. Chem. Front.* **2017**, *1*, 2111–2116.

[14] Wang, L. M.; Yao, Q.; Shi, W.; Qu, S. Y.; Chen, L. D. Engineering carrier scattering at the interfaces in polyaniline based nanocomposites for high thermoelectric performances. *Mater. Chem. Front.* **2017**, *1*, 741–748.

[15] Yang, T.; Cheng, T. X.; Zhou, G. D. Effects of Ag or Yb doping on thermoelectric properties of $Ca_3Co_{3.9}Cu_{0.1}O_{9-\delta}$. *Chem. J. Chin. Univ.* **2017**, *38*, 335–340.

[16] Caillat, T.; Carle, M.; Pierrat, P.; Scherrer, H.; Scherrer, S. Thermoelectric properties of $(Bi_xSb_{1-x})_2Te_3$ single crystal solid solutions grown by the T.H.M. method. *J. Phys. Chem. Solids* **1992**, *53*, 1121–1129.

[17] Zhang, Q.; Chere, E. K.; Sun, J. Y.; Cao, F.; Dahal, K.; Chen, S.; Chen, G.; Ren, Z. F. Studies on thermoelectric properties of n-type polycrystalline $SnSe_{1-x}S_x$ by iodine doping. *Adv. Energy Mater.* **2015**, *5*, 1500360.

[18] Yan, X.; Poudel, B.; Ma, Y.; Liu, W. S.; Joshi, G.; Wang, H.; Lan, Y. C.; Wang, D. Z.; Chen, G.; Ren, Z. F. Experimental studies on anisotropic thermoelectric properties and structures of n-type $Bi_2Te_{2.7}Se_{0.3}$. *Nano Lett.* **2010**, *10*, 3373–3378.

[19] Liu, W. S.; Zhang, Q. Y.; Lan, Y. C.; Chen, S.; Yan, X.; Zhang, Q.; Wang, H.; Wang, D. Z.; Chen, G.; Ren, Z. F. Thermoelectric property studies on Cu-doped n-type $Cu_xBi_2Te_{2.7}Se_{0.3}$ nanocomposites. *Adv. Energy Mater.* **2011**, *1*, 577–587.

[20] Soni, A.; Shen, Y. Q.; Yin, M.; Zhao, Y. Y.; Yu, L. G.; Hu, X.; Dong, Z. L.; Khor, K. A.; Dresselhaus, M. S.; Xiong, Q. H. Interface driven energy filtering of thermoelectric power in spark plasma sintered $Bi_2Te_{2.7}Se_{0.3}$ nanoplatelet composites. *Nano Lett.* **2012**, *12*, 4305–4310.

[21] Hong, M.; Chasapis, T. C.; Chen, Z. G.; Yang, L.; Kanatzidis, M. G.; Snyder, G. J.; Zou, J. n-type $Bi_2Te_{3-x}Se_x$ nanoplates with enhanced thermoelectric efficiency driven by wide-frequency phonon scatterings and synergistic carrier scatterings. *ACS Nano* **2016**, *10*, 4719–4727.

[22] Xu, B.; Feng, T. L.; Agne, M. T.; Zhou, L.; Ruan, X. L.; Snyder, G. J.; Wu, Y. Highly porous thermoelectric nanocomposites with low thermal conductivity and high figure of merit from large-scale solution-synthesized $Bi_2Te_{2.5}Se_{0.5}$ hollow nanostructures. *Angew. Chem.* **2017**, *129*, 3600–3605.

[23] Xu, B.; Agne, M. T.; Feng, T. L.; Chasapis, T. C.; Ruan, X. L.; Zhou, Y. L.; Zheng, H. M.; Bahk, J. H.; Kanatzidis, M. G.; Snyder, G. J. et al. Nanocomposites from solution-synthesized PbTe-BiSbTe nanoheterostructure with unity figure of merit at low-medium temperatures (500–600 K). *Adv. Mater.* **2017**, *29*, 1605140

[24] Zheng, G.; Su, X. L.; Li, X. R.; Liang, T.; Xie, H. Y.; She, X. Y.; Yan, Y. G.; Uher, C.; Kanatzidis, M. G.; Tang, X. F. Toward high-thermoelectric-performance large-size nanostructured BiSbTe alloys via optimization of sintering-temperature distribution. *Adv. Energy Mater.* **2016**, *6*, 1600595.

Pursuant to the DOE Public Access Plan, this document represents the authors' peer-reviewed, accepted manuscript.
The published version of the article is available from the relevant publisher.

[25] Chen, N.; Gascoin, F.; Snyder, G. J.; Müller, E.; Karpinski, G.; Stiewe, C. Macroscopic thermoelectric inhomogeneities in $(AgSbTe_2)_x(PbTe)_{1-x}$. *Appl*. *Phys*. *Lett*. **2005**, *87*, 171903.
[26] Mehta, R. J.; Zhang, Y. L.; Karthik, C.; Singh, B.; Siegel, R. W.; Borca-Tasciuc, T.; Ramanath, G. A new class of doped nanobulk high-figure-of-merit thermoelectrics by scalable bottom-up assembly. *Nat*. *Mater*. **2012**, *11*, 233–240.
[27] Zheng, Y.; Luo, Y. B.; Du, C. F.; Zhu, B. B.; Liang, Q. H.; Hng, H. H.; Hippalgaonkar, K.; Xu, J. W.; Yan, Q. Y. Designing hybrid architectures for advanced thermoelectric materials. *Mater*. *Chem*. *Front*. **2017**, *1*, 2457–2473.
[28] Zhang, G. Q.; Kirk, B.; Jauregui, L. A.; Yang, H. R.; Xu, X. F.; Chen, Y. P.; Wu, Y. Rational synthesis of ultrathin n-type Bi_2Te_3 nanowires with enhanced thermoelectric properties. *Nano Lett*. **2011**, *12*, 56–60.
[29] Tang, Z.; Wang, Y.; Sun, K.; Kotov, N. A. Spontaneous transformation of stabilizer-depleted binary semiconductor nanoparticles into selenium and tellurium nanowires. *Adv*. *Mater*. **2005**, *17*, 358–363.
[30] Bahk, J. H.; Shakouri, A. Minority carrier blocking to enhance the thermoelectric figure of merit in narrow-band-gap semiconductors. *Phys. Rev. B* **2016**, *93*, 165209.
[31] Cahill, D. G. Thermal conductivity measurement from 30 to 750 K: The 3ω method. *Rev. Sci. Instrum*. **1990**, *61*, 802–808.
[32] Kwon, S.; Zheng, J. L.; Wingert, M. C.; Cui, S.; Chen, R. K. Unusually high and anisotropic thermal conductivity in amorphous silicon nanostructures. *ACS Nano* **2017**, *11*, 2470–2476.
[33] Feser, J. P. Scalable routes to efficient thermoelectric materials. Ph.D. Dissertation, University of California, Berkeley, CA, USA, 2010.
[34] Zhang, Y. L.; Hapenciuc, C. L.; Castillo, E. E.; Borca-Tasciuc, T.; Mehta, R. J.; Karthik, C.; Ramanath, G. A microprobe technique for simultaneously measuring thermal conductivity and seebeck coefficient of thin films. *Appl*. *Phys*. *Lett*. **2010**, *96*, 062107.